Extending the use of normal hemispherical transmittance (T_NH) measurements by modeling 3D multiple scattering radiative transfer

Guillaume Foin, Laurent Brunel, Jean-François Cornet, Jérémi Dauchet, Fabrice Gros, Thomas Vourc'h

Extending the use of normal hemispherical transmittance (T_{NH}) measurements by modelling 3D multiple scattering radiative transfer

Guillaume Foin[a], Laurent Brunel[b], Jean-François Cornet[a], Jérémi Dauchet[a], Fabrice Gros[a], Thomas Vourc'h[a,*]

[a] *Université Clermont Auvergne, Clermont Auvergne INP, CNRS, Institut Pascal, F-63000 Clermont-Ferrand, France*
[b] *PhotonLyx Technology S.L., Santander, Spain*

Abstract

Spectrophotometers or optical benches using integrating spheres to measure normal-hemispherical transmittance T_{NH} are widespread laboratory equipments. Although it is known that they cannot be used for "highly turbid" samples, because multiple scattering may lead transmitted radiation to miss the entrance of the integrating sphere, very little is generally known about their exact validity range. Here we present a method to characterize the validity range of *any* such spectrophotometer and observe that most of them fail to measure T_{NH} for scattering optical thickness above 0.25 (*i.e.* for $T_{NH} < 0.9$ in the case of non absorbing media with $g = 0$). We also show how it is possible to continue using spectrophotometers even outside their T_{NH} measurement validity range, without any calibration, thanks to a proper simulation of radiative transfer and geometrical optics. We make available the corresponding radiative transfer simulation tools as open access codes, that have been developed for a straightforward implementation on a wide range of experimental setups. The method is validated on three different spectrophotometers or optical benches using standardized latex microspheres, then its practical implementation is illustrated in the case of semi-conductor particles and photosynthetic microalgae. Errors in analysis arising from the misuse of such optical devices are discussed throughout the article.

Preprint submitted to Journal of Quantitative Spectroscopy and Radiative Transfer

Final article available at https://doi.org/10.1016/j.jqsrt.2024.109124

Data are available at https://doi.org/10.57745/BVMFZ1

Keywords:
spectrophotometry, normal-hemispherical transmittivity, radiative transfer, turbid media, multiple scattering, geometrical optics, complex geometry, Monte Carlo Method

1. Introduction

Spectrophotometry is concerned with the quantitative analysis of reflectance and transmittance measurements on a sample, as a mean to investigate (or measure) the properties defining absorption and scattering of radiation within media. These radiative properties are the absorption coefficient, the scattering coefficient and the single-scattering phase function. Our study is motivated by two distinct uses of spectrophotometry:

1. a multi-scale multi-physics model is constructed to design and optimize a process (for example a photoreactor) involving electromagnetism to determine radiative properties of particles, radiative transfer within a suspension of such particles, heat transfer, charge-carrier transport, (photo)chemical reaction and so on [1, 2, 3, 4, 5, 6, 7, 8]. In this case, spectrophotometry is used to validate separately the first part of the model involving radiative properties and radiative transfer only, by comparing intermediate model results with measurements on a sample (see the references cited above).
2. the radiative properties of a material are determined from inversion of spectrophotometry measurements [9, 10, 11, 12, 13, 14].

Both cases require a direct model predicting the signal that should be measured for a sample with given thickness and radiative properties. Here we focus on the experiments and direct model; the subsequent question of inversion is treated elsewhere [14]. Such direct model principally involves the radiative transfer equation (RTE), and possibly geometrical optics at the interfaces.

The case of samples that only absorb radiation is quite straightforward, using standard normal-normal transmittance measurements. Collimated radiation incident on the sample is not deviated by it and we can ensure that the transmitted fraction always reach a sensor facing the source. Moreover, the RTE solution for this configuration is simply the Beer-Lambert-Bouguer exponential law, and inversion is straightforward taking the logarithm of the transmittance. The present work addresses situations where the scattering

properties of turbid media are of interest, which is much more complex because:

- on the measurement side, it is non-trivial to control which part of the transmitted (or reflected) radiation is detected since scattering modifies propagation directions, as a function of optical thickness. This question is usually addressed by using dedicated apparatus such as integrating spheres (to measure normal-hemispherical transmittance and/or reflectance) [1, 6, 7, 10] or nephelometers (to measure directional transmittance) [13, 15].
- simple analytical and rigorous RTE solution is no more available.

Here we focus on the most common approach: the measure of normal-hemispherical transmittance T_{NH} thanks to integrating spheres that are commercially available (the use reflectance is outside the scope of this article). In this case, the aim of integrating spheres is to capture transmitted radiation exiting the sample in every direction (Fig. 1). But these devices have a certain validity range in terms of scattering optical thickness above which they do not measure the T_{NH} anymore [12, 16]. Indeed, if multiple-scattering optical paths explore a large region within the sample, photons may for example miss the entrance of the integrating sphere either because they interact with the side faces of the cuvette prior to reach the exit face, or because the integrating sphere does not cover the whole exit face (see Fig. 1). Even if a special attention is devoted to design instruments with extended validity range [1, 6] by using cuvettes with large dimensions in the plane perpendicular to incident radiation, by using integrating spheres with large diameters, *etc.*, there is always a usage limit, as illustrated in Section 7.2.

The first difficulty that is addressed in this article is the fact that very little information is available about the validity range of spectrophotometers measuring normal-hemispherical transmittance, as a function of scattering optical thickness. Therefore, it is difficult to ensure that experiments are performed in the right conditions. We propose a generic methodology to characterize the validity range of any such device, and apply it to different experimental configurations: i) a high-accuracy optical bench using large cuvettes and a large integrating sphere, ii) a commercial spectrophotometer with a small integrating sphere accessory using standard 10x10 mm cuvettes, iii) a fast prototyped spectrophotometer using 3D printing.

The second difficulty that is addressed is encountered when the targeted application falls outside of the validity range of available devices. It can be the case in situation 1 mentioned above, where one wants to validate the radiative part of a model at the optical thickness corresponding to the final application, or in situation 2, where inversion requires to work at an optical thickness such that the measurements are sensitive to the radiative properties that one wants to retrieve. For those cases, we make available a methodology and open access simulation tools allowing to use T_{NH} measurement devices outside of their validity range, from intermediate to high optical thickness, without using any calibration on reference samples.

The proposed approach relies on the accurate simulation of the signal

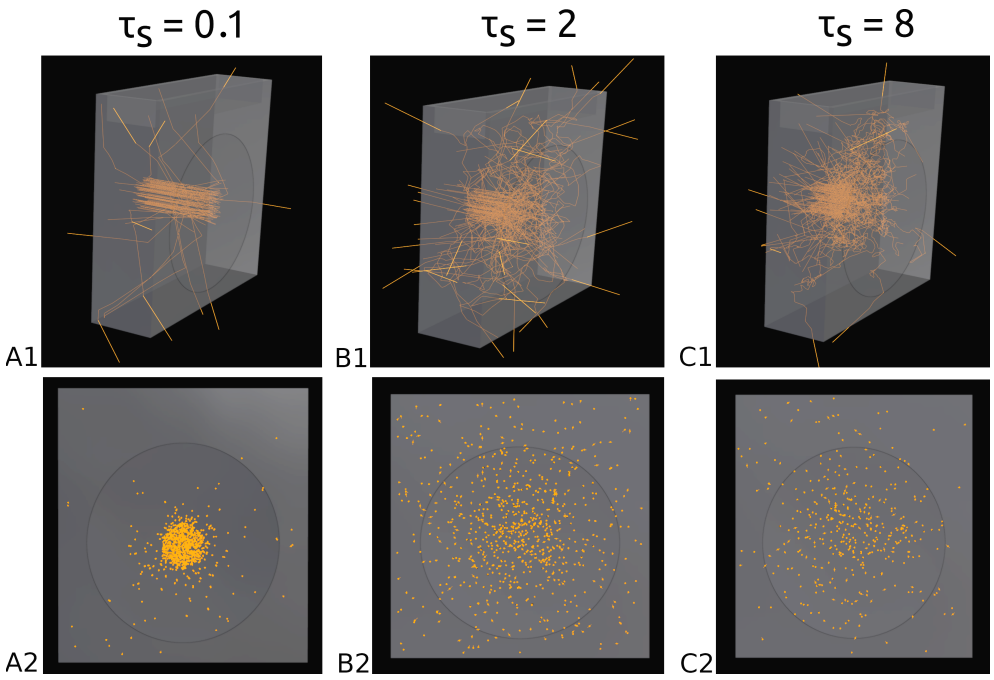

Figure 1: Optical paths in the cuvette of the experimental setup 1 (see Section 2), as sampled by the Monte Carlo radiative transfer algorithm in Section 3.4. Row 1 presents a side view of the cuvette with incident radiation on the left and integrating sphere entrance on the right. Row 2 presents a rear view of the cuvette with optical paths exit points shown in orange; the integrating sphere entrance is represented by a circle. The scattering optical thickness is $\tau_s = 0.1$ in Column A, $\tau_s = 2$ in Column B and $\tau_s = 8$ in Column C (see Eq. 12 for τ_s definition).

that is measured by the instrument. When working within the validity range of the instrument (standard case), the measured T_{NH} must be compared with the RTE solution in a one-dimensional slab. When working outside of the validity range, the T_{NH} cannot be measured precisely anymore and the three-dimensional complex geometry of the instrument, as well as geometrical optics at interfaces, must be included in the RTE solution in order to build a model that properly links the radiative properties of the sample to the measurements. Such approaches are reported in the literature, using analytical approximate solutions [17] or numerical Monte Carlo solution [18]. Those studies demonstrated the proof of concept for this modelling approach, but to the best of our knowledge, simulation tools and codes have been developed on a case by case basis, for specific devices, and they are not available to a large community. Building upon these works, our aim here is to provide a generic protocol using Free/Libre and Open Source Software (FLOSS) that can be implemented by a large community working on diverse experimental setups. We argue that this is possible because FLOSS RTE solvers are now mature enough to be used by non specialists and therefore, simulating an optical bench outside its validity range is in practice not more complicated than simulating a slab to estimate the T_{NH}. Here we use the Starlyx solver [19], that takes benefit of recent advances in computer graphics research, in the framework of physically based rendering [20]. In the present context, two major advantages of this computer science approach are:

- the description of each experimental setup (the source, sample, sensor, materials... that is the equivalent of the *scene* produced by artists in the context of computer graphics) is performed in a file that is totally independent from the part of the code that solves the RTE in that scene. This allows a clear articulation between scientific programming and the pragmatic use of the solver by spectroscopists (or artists) [21]. Therefore, i) it is straightforward to use Starlyx to simulate many different configurations, without being a Monte Carlo expert and ii) the components within Starlyx are validated, maintained and improved by a community pooling their efforts, despite different application motivations [22].

- Computer graphics tools and libraries allow highly efficient RTE numerical solution, in particular with CPU times that are fundamentally insensitive to the geometric complexity of the device [23]. This is quite important i) when designing experimental setups, which requires

to simulate diverse configurations to decide which one will be implemented, and ii) when inverting radiative properties from measurements, which requires to solve the direct model many times.

We make the codes used in this article freely available to the reader, under GPLv3 license.

First, the three representative devices that we use for illustration are presented in Section 2. Second, the model and its numerical solution are presented in Section 3. Then, our methodology is presented in Section 4, validated in Section 5 and discussed in Section 6. Finally, in Section 7, this methodology is implemented i) to produce the T_{NH} measurement validity range of the three studied devices and ii) to illustrate how it is possible to continue using a spectrophotometer even outside its validity range.

2. Experimental setups

This section provides details about the three representative spectrophotometers that are studied in the present paper.

2.1. Experimental setup 1: high accuracy optical bench

This device is based on a FLX-Xenius spectrofluorimeter from Safas Monaco, using a high energy pulsed Xenon lamp, connected to a 152 mm diameter integrating sphere manufactured by Labsphere (see Figure 2). The internal surface of the integrating sphere is coated with 99% light-reflecting Spectralon®. The diameter of the aperture is 32.7 mm. The diameter of the incident collimated beam is $d_{beam} = 7$ mm diameter disc. The dimensions of the QS quartz Suprasil® cuvette are $40 \times 38 \times 9.5$ mm (custom-made by Hellma Analytics).

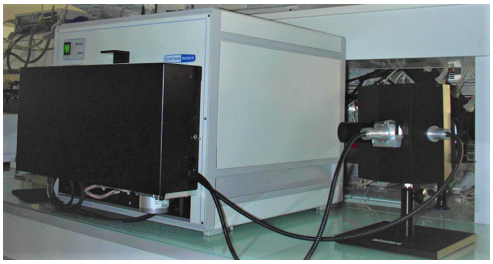

(a) Optical bench

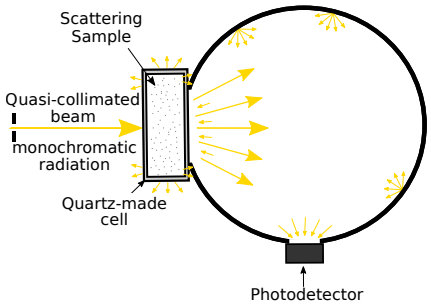

(b) Integrating sphere

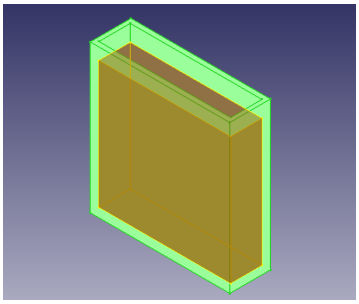

(c) Perspective view of the cuvette

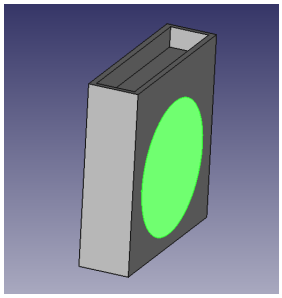

(d) 3D model

Figure 2: Experimental setup 1: high accuracy optical bench. **a)** Picture of the optical bench, with spectrofluorometer on the left, connected, thanks to optical fibers, to the integrating sphere on the right; **b)** Sketch of the sample and the integrating sphere; **c)** CAD geometry of the cuvette: air-quartz interface in green, liquid-quartz interfaces in orange, air-liquid interface is not shown here; **d)** the disc-shape surface represents the entrance of the integrating sphere at the rear of the cuvette. The CAD file is provided in [24].

2.2. Experimental setup 2: commercial spectrophotometer with integrating sphere accessory

For this setup, we have chosen a typical example of worldwide commercially available instruments. This spectrophotometer is a UV-2600i from Shimadzu, with the integrating sphere accessory ISR-2600 (see Figure 3a). The sphere aperture is rectangular (see Figure 3b). The source is a collimated rectangular beam with dimensions 2.5×3.75 mm. The dimensions of the QS quartz Suprasil® cuvette are 10×40×10 mm (Hellma Analytics).

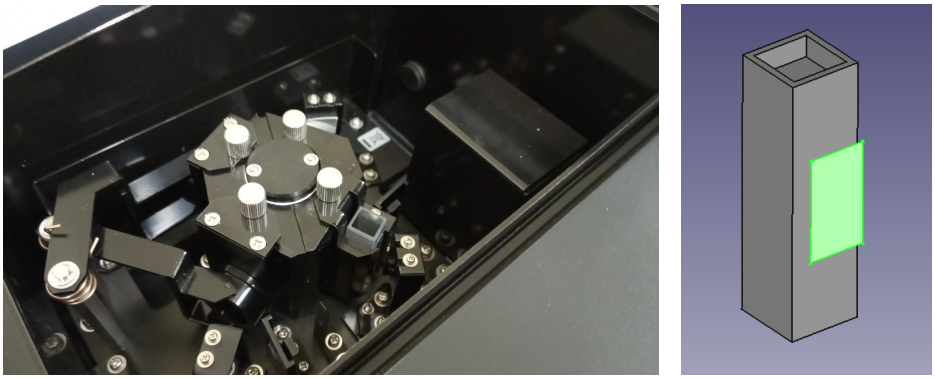

(a) Optical bench (b) 3D model

Figure 3: Experimental setup 2: commercial spectrophotometer. **a)** Picture of the optical bench. **b)** CAD geometry of the cuvette and the entrance of the integrating sphere (in green). The CAD file is provided in [24].

2.3. Experimental setup 3: Device derived from LyxS prototype

The third spectrophotometer is derived from the LyxS prototype [14] designed by PhotonLyX (see Figure 4). It has been built by PhotonLyX Technology using 3D printing and fast prototyping techniques. The integrating sphere is coated with white paint formulated with acrylic medium and Titane Dioxyde particles. The sphere aperture is a disk of 10 mm diameter centered on the rear face of the cuvette. The diameter of the incident collimated beam is 2.5 mm. The dimensions of the polystyrene cuvette are 10×40×10 mm (Greiner Macro-Cuvette 4 mL, ref n° 614101) .

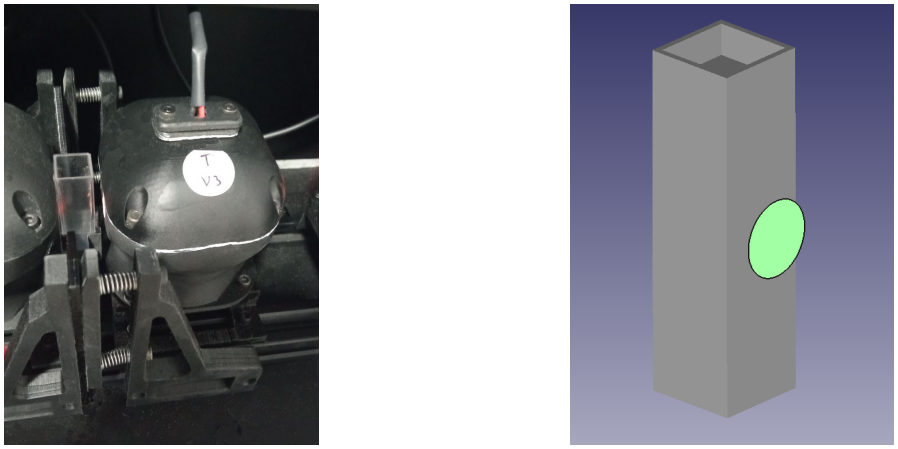

(a) Overview (b) 3D model

Figure 4: Experimental setup 3: device derived from LyxS prototype [14]. **a)** Picture of the optical bench. **b)** CAD geometry of the cuvette and the entrance of the integrating sphere (in green). The CAD file is provided in [24].

3. Model

This section will describe the 3D radiative transfer model which is solved to derive the signal delivered by a spectrophotometer. The equations in this model are the same whatever is the spectrophotometer, the only difference lies in the device geometry in which the model is solved (see for example the devices presented above). Hereafter we focus on the typical configuration presented on Figure 5: a sample is placed in a cuvette, which is illuminated with a collimated source. A sensor placed at the rear of the sample measures the light intensity collected after radiation has crossed the sample.

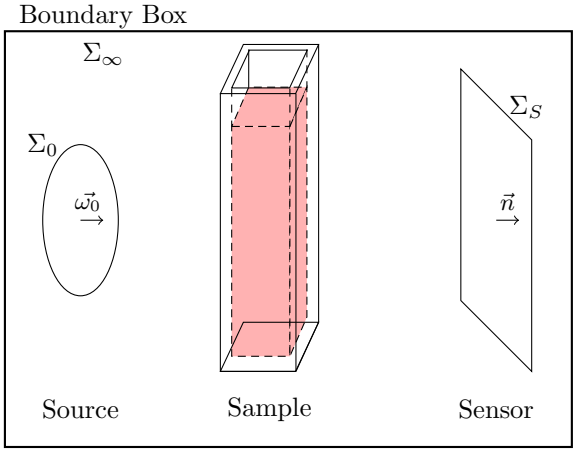

Figure 5: Typical experimental configuration for spectrophotometry measurements.Shapes of source and sensor are arbitrary; they must be specified for each experimental setup.

3.1. Radiative transfer equation

In the volume of the sample, spectral light intensity $I_\lambda(\boldsymbol{x}, \boldsymbol{\omega})$ at a position $\boldsymbol{x}$ in a direction $\boldsymbol{\omega}$ obeys the steady-state and source-free Radiative Transfer Equation (RTE) [25]:

$$\begin{aligned} \boldsymbol{\omega} \cdot \boldsymbol{\nabla} I_\lambda(\boldsymbol{x}, \boldsymbol{\omega}) = & -k_{s,\lambda} I_\lambda(\boldsymbol{x}, \boldsymbol{\omega}) - k_{a,\lambda} I_\lambda(\boldsymbol{x}, \boldsymbol{\omega}) \\ & + \int_{4\pi} k_{s,\lambda} p_{\boldsymbol{\Omega},\lambda}(\boldsymbol{\omega}|\boldsymbol{\omega}') I_\lambda(\boldsymbol{x}, \boldsymbol{\omega}') \, d\boldsymbol{\omega}' \end{aligned} \tag{1}$$

where $k_{s,\lambda}$ is the spectral scattering coefficient, $k_{a,\lambda}$ the spectral absorption coefficient, and $p_{\boldsymbol{\Omega},\lambda}$ the single-scattering phase function. These three parameters define the radiative properties of the sample.

3.2. Boundary conditions

At the source. The light source is considered as a collimated beam in the direction $\boldsymbol{\omega_0}$, with spectral surface flux density $q_{0,\lambda}$ homogeneous on the emitting surface Σ_0 (whose area is denoted A_0). In this case, the spectral power of the source is $Q_{0,\lambda} = A_0 \, q_{0,\lambda}$. Boundary conditions are written as:

$$I_\lambda(\boldsymbol{y} \in \Sigma_0, \boldsymbol{\omega}) = \begin{cases} \frac{Q_{0,\lambda}}{A_0} \text{ for } \boldsymbol{\omega} = \boldsymbol{\omega_0} \\ 0 \text{ otherwise} \end{cases} \tag{2}$$

At the sensor. The sensor is described by a surface Σ_S, whose normal vector $\boldsymbol{n}$ is pointing in the direction opposite to the sample. Typically, if the sensor is an integrating sphere, Σ_S is considered as a disc representing the entrance of the sphere. Note that Σ_S might also be an exit for radiation coming from inside the sphere. Indeed, radiation that has entered the sphere can go back out after multiple reflections (see Fig 2b). To account for this case, Σ_S is an absorbing and reflecting surface, with reflectivity $\rho_{S,\lambda}$ and a distribution function for reflection direction $p_r(\boldsymbol{\omega}, \boldsymbol{\omega'})$. Incident radiation is either absorbed by the sensor, and therefore detected, or reflected. In the following, we consider Lambertian-reflection $p_r = \frac{1}{\pi}$ for the sensors. The value of $\rho_{S,\lambda}$ mainly relies upon the ratio between the diameter of the entrance of the sphere and the diameter of the sphere itself, and is expected to tend to 0 as this ratio decreases (which corresponds to an ideal case). Note that this reflectivity of the sensor is completely different of the reflectivity of the sphere coating, which is close to 1.

Hence the boundary condition writes:

$$I_\lambda\left(\boldsymbol{y} \in \Sigma_S, \boldsymbol{\omega}\right) = \int\limits_{\boldsymbol{\omega'}\cdot\boldsymbol{n}>0} \rho_{S,\lambda} I_\lambda\left(\boldsymbol{y}, \boldsymbol{\omega'}\right) p_r(\boldsymbol{\omega}, \boldsymbol{\omega'})\, \boldsymbol{\omega'}\cdot\boldsymbol{n}\, d\boldsymbol{\omega'}, \text{for} \boldsymbol{\omega}\cdot\boldsymbol{n}(\boldsymbol{y}) < 0 \quad (3)$$

The sensor is considered as a perfect absorber on its side facing the opposite direction of the sample (here, the sensor is the entrance of the integrating sphere, as defined in Figure 5) .

On the boundary box. To close the system, a boundary box is defined, whose surface is denoted Σ_∞, with normal vector pointing towards the inside of the system. This box is considered as a black body at 0 Kelvin:

$$I_\lambda\left(\boldsymbol{y} \in \Sigma_\infty, \boldsymbol{\omega}\right) = 0 \ \text{ for } \boldsymbol{\omega}\cdot\boldsymbol{n}(\boldsymbol{y}) > 0 \quad (4)$$

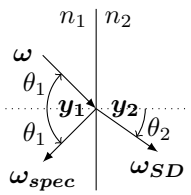

Figure 6: Notations for geometrical optics at location $\boldsymbol{y}$ on the interface between two media with refractive index n_1 and n_2 respectively. $\boldsymbol{y}_1$ is the location in medium 1 and $\boldsymbol{y}_2$ in medium 2. For a given direction $\boldsymbol{\omega}$ forming an angle θ_1 with the normal, the specular reflection direction is $\boldsymbol{\omega}_{spec}$ and the refraction direction, noted $\boldsymbol{\omega}_{SD}$, forms an angle θ_2 with the normal.

At the interface Σ_I between two media with different refractive index. At the interface between the sample, air or cuvette material, light is refracted and reflected according to the laws of geometrical optics [25]:

$$I_\lambda\left(\boldsymbol{y}_1 \in \Sigma_I, -\boldsymbol{\omega}\right) = \rho_{1\to 2,\lambda}(\boldsymbol{\omega}_{spec}) I_\lambda\left(\boldsymbol{y}_1, -\boldsymbol{\omega}_{spec}\right) + \left(1 - \rho_{2\to 1,\lambda}(\boldsymbol{\omega}_{SD})\right)\left(\frac{n_2}{n_1}\right)^2 I_\lambda\left(\boldsymbol{y}_2, -\boldsymbol{\omega}_{SD}\right) \quad (5)$$

where

- $\boldsymbol{y}_1$ and $\boldsymbol{y}_2$ are the locations at the interface, in the medium 1 and 2 respectively; other notations are defined in Fig. 6.
- Refraction direction is provided by Snell-Descartes law

$$n_{1,\lambda}\sin(\theta_1) = n_{2,\lambda}\sin(\theta_2) \quad (6)$$

- Reflectivity $\rho_{i\to j}(\boldsymbol{\omega}_{inc})$ for incident radiation incoming from medium i with direction $\boldsymbol{\omega}_{inc}$ towards medium j, is provided by Fresnel law for unpolarized light when the incident angle θ_i is below the *angle for total reflection* θ_m; radiation is totally reflected beyond θ_m:

$$\rho_{i\to j,\lambda} = \begin{cases} \frac{1}{2}\left(\frac{n_{i,\lambda}\cos(\theta_i) - n_{j,\lambda}\cos(\theta_j)}{n_{i,\lambda}\cos(\theta_i) + n_{j,\lambda}\cos(\theta_j)}\right)^2 + \frac{1}{2}\left(\frac{n_{i,\lambda}\cos(\theta_j) - n_{j,\lambda}\cos(\theta_i)}{n_{i,\lambda}\cos(\theta_j) + n_{j,\lambda}\cos(\theta_i)}\right)^2 \text{ for } \theta_i < \theta_{m,\lambda} \\ 1 \text{ for } \theta_i \geq \theta_{m,\lambda} \end{cases} \quad (7)$$

with $n_{i,\lambda}\sin(\theta_{m,\lambda}) = n_{j,\lambda}$.

3.3. Signal delivered by the spectrophotometer

Our model aims at describing the signal delivered by the spetrophotometer, *i.e* the value between 0 and 1 obtained after an experiment. This section aims at detailing how we build this observable.

The electric signal $\mathcal{S}_\lambda$ measured by a spectrophotometer is proportional to the flux absorbed on the sensor: $\mathcal{S}_\lambda = \alpha\, Q_\lambda^{abs}$, where α is a proportionality coefficient that depends on the photodetector and Q_λ^{abs} the radiative flux absorbed by the sensor.

$$Q_\lambda^{abs} = (1 - \rho_{S,\lambda}) \int_{\Sigma_S} d\boldsymbol{y} \int_{\boldsymbol{\omega}\cdot\boldsymbol{n}>0} I_\lambda(\boldsymbol{y}, \boldsymbol{\omega})\, \boldsymbol{\omega}\cdot\boldsymbol{n} d\boldsymbol{\omega} \tag{8}$$

The resolution of Eqs 1 to 7 enables to compute Q_λ^{abs}.

The value of α is not required because the signal delivered by the spectrophotometer is the ratio of the signal $\mathcal{S}_{sample}$ measured on the sample divided by the signal $\mathcal{S}_{blank}$ measured on a blank sample (providing the baseline):

$$\varphi_\lambda = \frac{\mathcal{S}_{sample,\lambda}}{\mathcal{S}_{blank,\lambda}} = \frac{Q^{abs}_{sample,\lambda}}{Q^{abs}_{blank,\lambda}} \tag{9}$$

In the following φ_λ will be referred to as the *device model*.

Note that radiative transfer being a linear physics, both $Q^{abs}_{sample,\lambda}$ and $Q^{abs}_{blank,\lambda}$ are proportional to the power $Q_{0,\lambda}$ emitted by the source. As a consequence, the signal delivered by the spectrophotometer is independent of $Q_{0,\lambda}$ and we will use $Q_{0,\lambda} = 1$ in our simulations.

Estimation of the normal-hemispherical transmittance T_{NH} of the sample inside the cuvette. The above definition of φ_λ is fully consistent with the definition of T_{NH}, under the following assumptions:

- The sensor is a perfect absorber (*i.e* $\rho_S = 0$)
- The sample is an infinite slab; the source covers the front face of this slab and the sensor covers the rear side of this slab (*i.e* Σ_0 is the infinite plane on one side of the slab ; Σ_S is the infinite plane on the other side.)
- According to the standard spectrophotometry practice, we work with the transmittance of the sample inside the cuvette (*i.e* $T_{NH} = \exp(-k_a\, E)$ for a purely absorbing medium). Hence, both the source and the sensor are placed on the *internal* side of the sample.

In this case $Q^{abs}_{blank,\lambda} = Q_{0,\lambda}$, hence Eq. 9 becomes:

$$\varphi_\lambda = T_{NH} = \frac{\int_{\Sigma_S} d\boldsymbol{y} \int_{\boldsymbol{\omega}\cdot\boldsymbol{n}>0} I_\lambda(\boldsymbol{y},\boldsymbol{\omega})\, \boldsymbol{\omega}\cdot\boldsymbol{n}\, d\boldsymbol{\omega}}{Q_{0,\lambda}} \tag{10}$$

3.4. Monte Carlo solution

The above set of equations is solved using Starlyx software [19]. Starlyx is freely available and is distributed along with practical examples that include the material to run simulations of this article (see the folder named *examples*). Basically, starlyx structures the data provided by the user to describe his setup (which is named the *scene*) and implements a Monte Carlo radiative transfer algorithm in this scene.

Description of the scene. The geometry of the device (source, sample, sensor...) is defined by surfaces described in computer aided design (CAD) files such as .obj or .stl files. The surface and volume properties associated with these geometries are described in a .xml file, using a grammar presented in Starlyx documentation (see the examples that can be downloaded along with Starlyx, as well as [24]).

Monte Carlo algorithm. The sampling procedure in Algorithm 1 is implemented N times, to sample MC realizations $w_{n=1,2...,N}$. Unbiased estimation of the flux absorbed at the sensor is then calculated as

$$Q^{abs} = \frac{1}{N}\sum_{n=1}^{N} w_n \tag{11}$$

with uncertainty provided by the standard deviation of the w_n.

4. Methods

This section aims at describing the methodology followed in this paper to compare experimental measurements with the results of the model described in section 3.

Experimental data are acquired following the standard practice of spectrophotometry: a baseline is recorded using a cuvette filled with the solvent only, then measurements relative to this baseline are performed using a cuvette filled with the sample (particles in suspension within the solvent).

Simulations are obtained as follows, keeping the baseline practice:

Algorithm 1: Flux absorbed at the sensor (see Fig. 5)

Data: λ, a scene.
Result: A MC realization w.

Uniform sampling of an emission location $\boldsymbol{x}_0$ on the source surface Σ_0.
Set the emission direction to $\boldsymbol{\omega}_0$;
$j \leftarrow 0$
Sample an extinction length according to $p_{L_j,i}(l_j) = (k_{a,i,\lambda} + k_{s,i,\lambda}) \exp(-(k_{a,i,\lambda} + k_{s,i,\lambda})l_j)$, where i is the index of the current volume, either air, cuvette material or the suspension (note that l_j is infinite everywhere except inside the suspension).
Compute the first intersection $\boldsymbol{y}_{j+1}$ between the ray (half line) starting at $\boldsymbol{x}_j$ in direction $\boldsymbol{\omega}_j$ and the geometry (*i.e.* the union of all surfaces $\Sigma_\infty \cup \Sigma_I \cup \Sigma_S \cup \Sigma_0$).
if $||\boldsymbol{y}_{j+1} - \boldsymbol{x}_j|| < l_j$ `// Interaction with a surface`
then
  if $\boldsymbol{y}_{j+1} \in \Sigma_\infty \cup \Sigma_0$ `// the source or the boundary box`
  then
    The algorithm returns $w = 0$ and stops.
  else if $\boldsymbol{y}_{j+1} \in \Sigma_S$ `// the sensor`
  then
    Uniformly sample a realization r_{j+1} in the unit interval.
    if $r_{j+1} > \rho_S$ `// absorption`
    then
      The algorithm returns $w = Q_{0,\lambda}$ and stops.
    else
      Lambertian sampling of the reflection direction $\boldsymbol{\omega}_{j+1}$. `// reflection`
      $\boldsymbol{x}_{j+1} \leftarrow \boldsymbol{y}_{j+1}$; $j \leftarrow j + 1$; Go to line 4.
    end
  else
    $\boldsymbol{x}_{j+1} \leftarrow \boldsymbol{y}_{j+1}$ `//` $\boldsymbol{y}_{j+1} \in \Sigma_I$`, an interface between two media, see Fig. 6`
    Uniformly sample a realization r_{j+1} in the unit interval.
    if $r_{j+1} < \rho_\lambda$ `// Reflection according to Eq. 7`
    then
      Direction is set to the specular direction: $\boldsymbol{\omega}_{j+1} \leftarrow \boldsymbol{\omega}_{j,spec}$.
      $j \leftarrow j + 1$; Go to line 4.
    else
      Set i to the index of the new volume we entered. `// Refraction, see Eq. 6`
      Propagation direction is set to the refraction direction: $\boldsymbol{\omega}_{j+1} \leftarrow \boldsymbol{\omega}_{j,SD}$.
      $j \leftarrow j + 1$; Go to line 4.
    end
  end
else
  $\boldsymbol{x}_{j+1} \leftarrow \boldsymbol{x}_j + l_j\, \boldsymbol{\omega}_j$ `// Interaction within the volume`
  Uniformly sample a realization a_{j+1} in the unit interval.
  if $a_{j+1} < \dfrac{k_{s,i,\lambda}}{k_{a,i,\lambda} + k_{s,i,\lambda}}$ `// Scattering`
  then
    Sample $\boldsymbol{\omega}_{j+1}$ according to the phase function $p_{i,\lambda}(\boldsymbol{\omega}_{j+1}|\boldsymbol{\omega}_j)$.
    $j \leftarrow j + 1$; Go to line 4.
  else
    The algorithm returns $w = 0$ and stops. `// Absorption`
  end
end

1. Definition of the surfaces that constitute the geometry (source, sensor, cuvette). In this paper, all surfaces are defined by `.obj` files that have been produced using FreeCAD [26] and Blender [27] softwares and that are made available in [24] and in the *examples* folder downloaded with Starlyx [19].
2. Production of a scene named `empty.xml` corresponding to the device in the absence of cuvette. Every refractive indexes are set to 1 and no radiative properties are indicated. Simulation in this scene results in the flux Q^{abs}_{empty} absorbed at the sensor in the absence of cuvette. Note that if the reflectivity ρ_S of the sensor is zero, if the source is facing the sensor and if the source is smaller than the sensor, the entire flux Q_0 emitted by the source is absorbed at the sensor, and since we use $Q_0 = 1$ in our simulations (see Sec. 3.3), we should obtain $Q^{abs}_{empty} = Q_0 = 1$. Nevertheless, other configurations are possible (in particular when $\rho_S \neq 0$).
3. Starting from `empty.xml`, the refractive index of the cuvette is now indicated in a new scene named `cuvette.xml` (other refractive indexes remain set to 1). The result obtained with this scene is noted $Q^{abs}_{cuvette}$.
4. Identification of the reflectivity of the sensor ρ_S from an experimental measurement performed on an empty cuvette:
   (a) Measure the signal $\mathcal{M}$ obtained on an *empty cuvette* (*i.e* filled with air), relative to a baseline recorded *without cuvette*.
   (b) Run a minimization procedure by modifying ρ_S in both `empty.xml` and `cuvette.xml` files, until $\frac{Q^{abs}_{cuvette}}{Q^{abs}_{empty}} = \mathcal{M}$. For the three setups described in section 2, we have found respectively $\rho_S = 0.3$, $\rho_S = 0$ and $\rho_S = 0$. The value of 0.3 for the first apparatus is due to the large aperture of the sphere relatively to its diameter ($\frac{d_{aperture}}{d_{sphere}} \sim 20\%$, whereas it is less than 10% for the other devices).
   (c) Specify the value obtained for ρ_S in the `.xml` files.
5. Simulation of the baseline performed on a blank sample. Starting from `cuvette.xml`, the refractive index of the solvent is now indicated in a new scene named `blank.xml`. The result obtained with this scene is noted Q^{abs}_{blank}.
6. For each new experiment, starting from `blank.xml`, the radiative properties of the sample are now indicated in a new scene named `sample.xml`. The result obtained with this scene is noted Q^{abs}_{sample}. The signal φ delivered by the spectrophotometer is obtained from Eq. 9.

Note that only the last step is to be repeated for each experiment, all the previous ones are to be performed only once to characterize the optical bench itself.

5. Validation

The method presented in the previous section does not require any calibration process from a reference sample other than the cuvette itself. In this section, we carry out a direct model validation, comparing the signal model φ and experimental measurements obtained on standard polystyrene microspheres.

5.1. Materials

Three different media are involved: air, cuvette material and suspensions of polystyrene microspheres in water. The refractive index of air is equal to 1. Cuvettes are made of quartz for experimental setups 1 and 2, and of polystyrene for experimental setup 3. Spectral refractive index of quartz is calculated using Sellmeier dispersion equation, using empirical coefficients from [28]. Spectral refractive index of polystyrene is calculated using a modified Cauchy's equation, with dispersion coefficients obtained in [29]. The real part of water refractive index is taken from [30], and its imaginary part from [31].

Spherical standard particles (Applied microspheres MicroStandard™ series) with density $\rho = 1050$ kg/m^3 and refractive index $n = 1.59$ at 589 nm are used. Refractive index at other wavelengths is computed according to the dispersion coefficients from [29]. Three particle sizes are investigated: mean diameter 3.07, 4.96 and 9.88 μm, with coefficient of variation 1.5%, 1.6% and 2.7% respectively (in the following these particles will be named "3, 5 and 10 μm"). Size distribution is assumed Gaussian, with the above mean and standard deviation provided by the manufacturer. Radiative properties are obtained by ignoring the imaginary part of water refractive index and using the Lorenz–Mie code provided at `www.giss.nasa.gov/staff/mmishchenko`. Note that particles do not absorb in the considered spectral range, so that the absorption cross-section $\sigma_{a,\lambda}$ is equal to 0. Values of the scattering cross-section $\sigma_{s,\lambda}$ and asymmetry parameter g_λ of the phase function are provided in Table 1 (the Mie phase functions used in the simulations are tabulated for 500 angles).

Finally, the scattering coefficient $k_{s,\lambda}$ of a microspheres suspension with concentration C is $k_{s,\lambda} = C\,\sigma_{s,\lambda}$ and the absorption coefficient $k_{a,\lambda}$ is constructed based on the imaginary part κ_λ of water refractive index: $k_{a,\lambda} = \frac{4\pi\kappa_\lambda}{\lambda}$ (which provides slight attenuation between 700 and 750 nm).

5.2. Radiative transfer model validation

Figure 7 compares some representative experimental spectra with model results (obtained as described in Section 4, for a water-filled cuvette baseline) in the case of the three experimental setups described in Section 2.1. Table 1 provides validation results obtained at 589 nm only, but in a larger number of configurations (concentrations and particle sizes). Note that thanks to the Monte Carlo libraries that have been presented in the introduction, the same model is solved with the same algorithms for the three setups; only the geometric data is modified accordingly.

The model and experimental measurements are in agreement, with differences that are always below 5% for setups 1 and 2, and below 10% for setup 3 (see Tab. 1). At this level of accuracy, the model is fully validated.

Diameter		3 μm				5 μm				10 μm			
σ_s(m^2/kg)		870				543				290			
g		0.83				0.86				0.9			
C_m (g/L)		0.2	0.4	2	5	0.2	0.8	2	10	0.2	2	5	10
τ_S		0.29	0.58	2.92	7.30	0.15	0.60	1.51	7.54	0.06	0.57	1.43	2.86
T_{NH}		0.90	0.81	0.39	0.19	0.95	0.80	0.58	0.19	0.98	0.81	0.58	0.39
Setup 1	Exp	0.82	0.67	0.37	0.27	0.91	0.67	0.44	0.26	0.97	0.68	0.45	0.36
	φ	0.81	0.67	0.37	0.26	0.91	0.67	0.46	0.26	0.97	0.66	0.46	0.37
Setup 2	Exp	0.69	0.49	0.12	0.063	0.84	0.50	0.23	0.061	0.96	-	-	-
	φ	0.69	0.48	0.12	0.065	0.84	0.49	0.22	0.063	0.93	0.47	0.21	0.12
Setup 3	Exp	-	0.36	0.060	0.031	0.73	-	0.146	0.030	-	-	-	0.081
	φ	0.58	0.36	0.065	0.034	0.78	0.29	0.131	0.033	0.91	0.34	0.12	0.064

Table 1: Validation of the device model at $\lambda = 589$ nm for different particle diameters, concentrations C_m and experimental setups described in Section 2.1. Experimental results are provided in the row named Exp and model results in the row named φ (95% confidence interval of Monte Carlo calculations are always below 0.0015). Scattering cross-section σ_s and asymmetry parameter g obtained by Mie theory are indicated, as well as the scattering optical thickness τ_s and normal-hemispherical transmittance T_{NH} calculated for a 10 mm slab.

In order to prepare analysis that will be drawn in the following sections, we also assess the relevance of scaling the results as a function of scattering

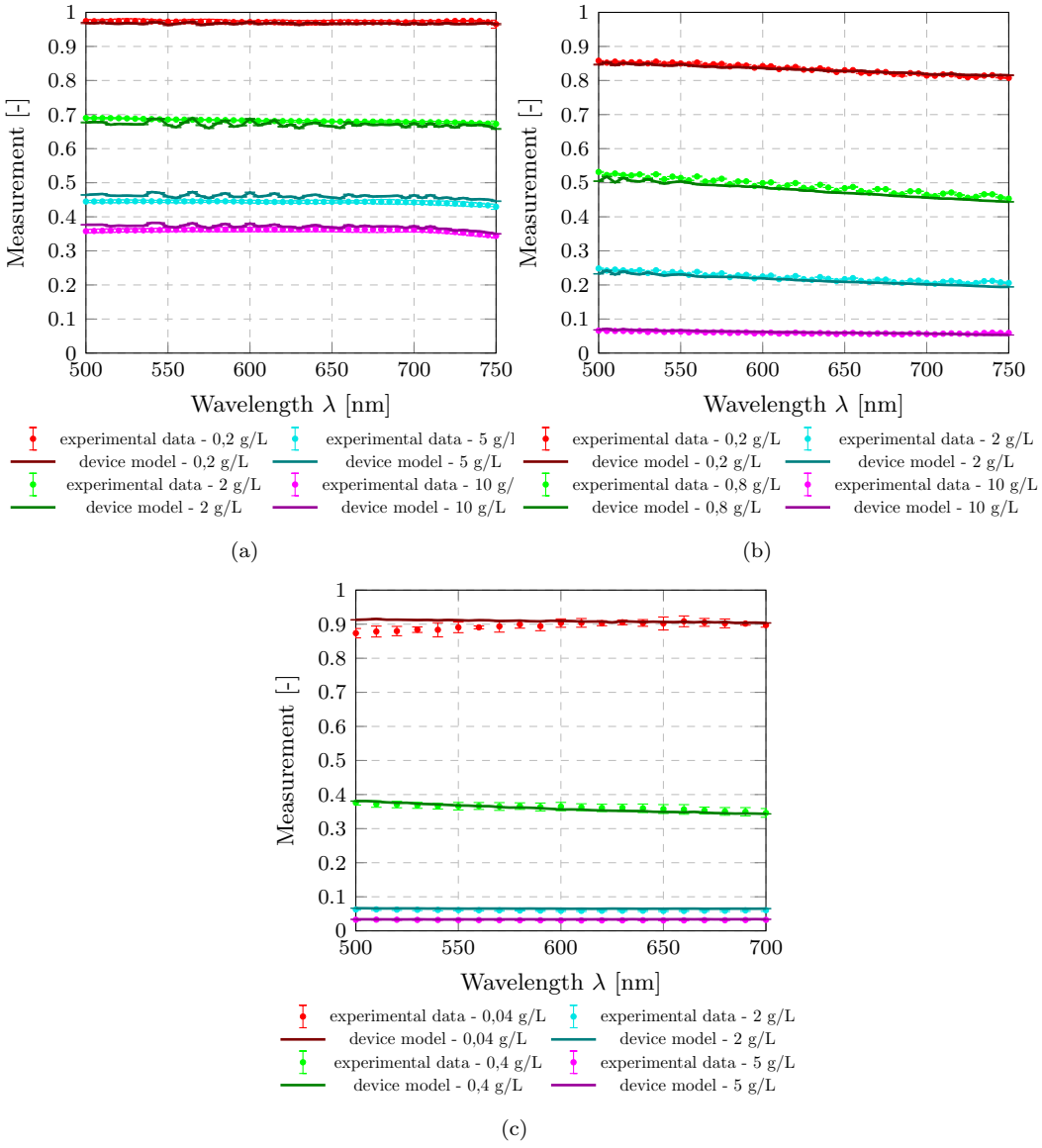

Figure 7: Spectral validation of the device model. a) Experimental setup 1, 10 μm particles (σ_s = 290 m^2.kg^{-1}, g =0.9). b) Experimental setup 2, 5 μm particles (σ_s = 543 m^2.kg^{-1}, g =0.86). c) Experimental setup 3, 3 μm particles (σ_s = 870 m^2.kg^{-1}, g =0.83). These radiative properties are provided for λ =590 nm, but are almost constant on the wavelength range. The 95% confidence interval of Monte Carlo calculations are indicated as error bars. Experimental data are obtained with the three experimental setups described in Section 2.1, each one analyzing a different size of microspheres, as provided in the legend of the sub-figures. Note that none of the experiments is used to calibrate the model.

optical thickness

$$\tau_s = k_s \, E \, (1 - g) \tag{12}$$

where E is the light path of the cuvettes (we use $E = 1\,cm$ in the following, according to our experimental setups). To do so, Figure 8 compares on the same graph, as a function of τ_s, the model and the 28 experiments from Table 1. The aim of this scaling is to compare different samples, in particular different particle types, with only one device model plot. For that purpose, we use the Henyey-Greenstein phase function in our simulations. Otherwise, we would have to compute model results for each Mie phase functions, *i.e.* for each particle size, as in Table 1. As a consequence, note that model results in Figure 8 are less accurate than those in Table 1, especially for the setup 3 between $\tau_s = 0.5$ and 3 where 10% differences are observed due to the phase functions difference. Meanwhile this scaling is adopted in the following to analyze a great variety of samples.

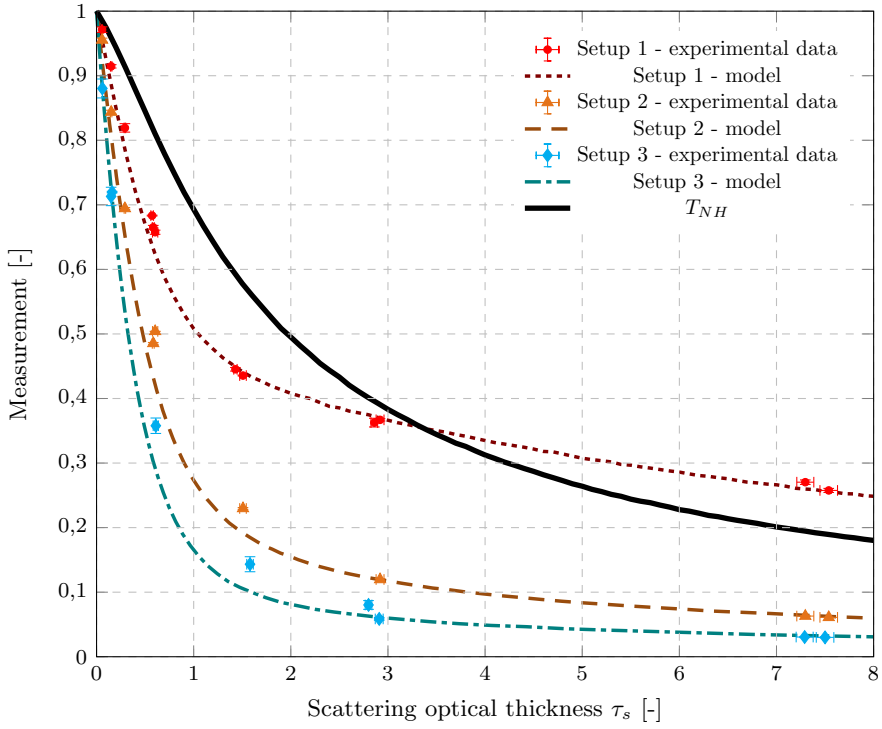

Figure 8: Scaling of the model as a function of scattering optical thickness and comparison with the 28 experiments from Table 1. Simulations use Henyey-Greenstein phase function with $g = 0.9$, whereas the Mie phase function for each particle type is used in Table 1 (giving different values of g). 95% confidence interval of Monte Carlo calculations are always below 0.0015. The three setups are detailed in Section 2.1. The normal-hemispherical transmittance T_{NH} of a 1 cm slab is plotted in black. The medium does not absorb radiation.

6. Discussion

On the one hand, validation results in previous section indicate that none of the three setups provides measurements corresponding to the normal-hemispherical transmittance T_{NH} for optical thickness τ_s above 0.2. On the other hand, our model φ that includes a description of the setups geometry, as well as geometrical optics, well describes the measurements up to $\tau_s \simeq 8$ (see Figs. 7, 8 and Table 1). This section aims at discussing these discrepancies between the T_{NH} and φ, through a sensitivity analysis to the different components of our model. For that purpose, Figure 9 presents the results obtained with different configurations of the model and shows how, by enriching

the model starting from the T_{NH}, experimental results are recovered.

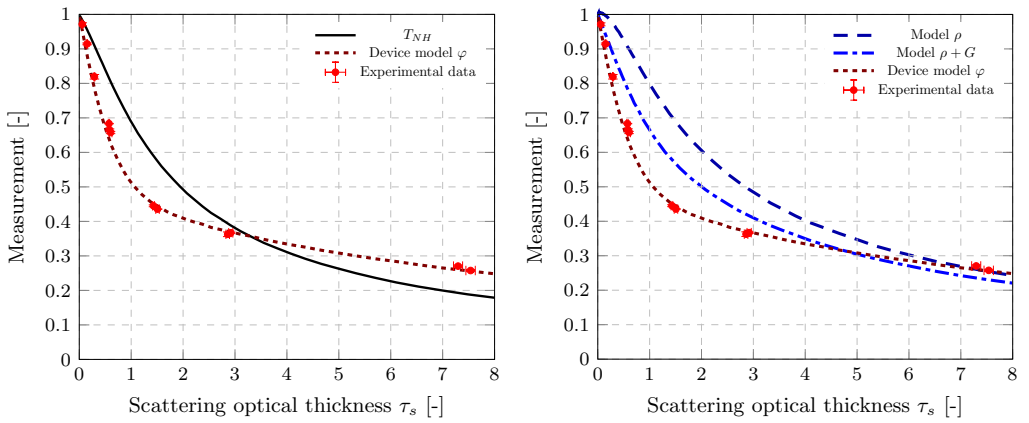

(a) (b)

Model	Sensor reflectivity	Setup geometry	Geometrical optics
T_{NH}			
Model ρ	X		
Model $\rho + G$	X	X	
Device model φ	X	X	X

(c)

Figure 9: Sensitivity analysis to the different components in the model φ, in the case of the experimental setup 1 (see Sec. 2.1). a) Experimental data against T_{NH} and device model φ as a function of scattering optical thickness. Standard water-filled cuvette baseline is used in both the experiments and φ (see Sec. 4). b) Results obtained with models of increasing accuracy, obtained by adding components from the T_{NH} computation: sensor reflectivity (integrating sphere), device geometry, geometrical optics. c) Description of the different model configurations used in a) and b): for each model, components taken into account are marked with an 'X'. 95% confidence interval of Monte Carlo calculations are always below 0.0015.

Normal-hemispherical transmittance T_{NH}. In Figure 9a, the **black** curve is the T_{NH}, which corresponds to simulations where neither the reflectivity of the sensor, the geometry nor geometrical optics is taken into account (see section 3.3). Numerically, this is either achieved with a specific code computing the normal-hemispherical transmittance, or by running our Starlyx simulation for a scene defining a very large cuvette and a very large sensor, and by setting the water and quartz refractive indexes to 1.0 (*i.e* the same value as air).

Effect of the sensor reflectivity ρ_S. Let us remind that ρ_S is introduced in order to account for radiation that would entered the integrating sphere and go back out after multiple reflections inside the sphere (see Fig 2b). For the experimental setup 1, we found $\rho_S = 0.3$ (see Sec. 4). The **dashed** curve in Figure 9b, labeled "Model ρ", is the simulation result for the same configuration as for T_{NH}, except that the sensor reflectivity is now considered. In comparison with the T_{NH}, this addition brings the model closer to experimental data at large τ_s, where reflected radiation have a chance to come back again inside the integrating sphere and be detected after multiple scatterings inside the sample, whereas it is not the case for the blank computation. On the other hand, it overestimates experimental measurements for smaller values of τ_s.

Effect of geometry. In the computation of the normal-hemispherical transmittance T_{NH}, there are only three issues for a photon coming from the source:

i reaching the sensor at $x = E$,
ii coming back by the front side at $x = 0$ after multiple scatterings in the medium,
iii being absorbed in the medium (in the case of absorbing media).

A first obvious difference between the computation of T_{NH} and the computation of φ is that the former is associated with a 1D slab geometry whereas in the latter, the sensor and the cuvette have finite dimension, so that two other issues are possible which lowers the signal (see Fig. 1):

i reaching the rear face of the cuvette at $x = E$ but missing the sensor due to its finite surface area,
ii escaping from the four lateral sides of the cuvette.

In Figure 9b, the **dotted** curve labeled "Model $\rho + G$" is based on "Model ρ", but this time the actual geometry of the cuvette and sensor is taken into account. Quartz and water refractive indexes are still equal to 1.0. By taking into account geometry, signal value is indeed lowered compared to Model ρ as radiation can leave the cuvette by its sides or by the rear face without interacting with the sensor. This enables to get closer to experimental measurements.

Effect of geometrical optics. The other difference between the T_{NH} model and φ is that the latter accounts for reflection and refraction at interfaces. The **dash-dotted** curve labeled "Device model φ" in Figs. 9a and 9b is the whole device model, which encompasses the effects of sensor reflectivity, device geometry and geometrical optics. The scene is the same as for "Model $\rho + G$" except that the refractive indexes of water and quartz are now taken to their actual value. This adds a reflectivity at the rear of the cuvette, before the sensor, which lowers the signal compared to "Model $\rho + G$" for $\tau_s < 5$. But on the other hand, a slight increase of the signal is observed compared to "Model $\rho + G$" at higher τ_s. This may be caused by the reflectivity at the sides and the front of the cuvette, that increases as multiple scattering modifies incidence angles at interfaces and therefore prevent radiation from exiting the cuvette (see Eq. 7). Overall, the three components of the model play a role of comparable importance in explaining the experimental results.

The baseline does not cancel the effects of geometrical optics. The experimental results in the present paper are obtained by applying the standard baseline practice, using a cuvette filled with solvent only (water here) as a blank sample. Performing such a baseline is classically used to cancel the effects of geometrical optics, but it only works at low scattering optical thickness τ_s. Indeed, to cancel the effect of reflection at the interfaces, geometrical optics must play a comparable role in the measure of the baseline signal $\mathcal{S}_{blank}$ and in the measure of the sample signal $\mathcal{S}_{sample}$. This is the case for non scattering samples, where the incidence angle of radiation on the interfaces is the same in both measures, hence the reflectivity at the interfaces is also the same (see Eq. 7), leading to a product of equal reflectivities that cancels in the ratio $\mathcal{S}_{sample}/\mathcal{S}_{blank}$ (see Eq. 9). But for scattering samples, despite the baseline, Figure 9b displays a significant impact of geometrical optics (compare "Model $\rho + G$" and "Device model φ"). This is due to multiple scattering within the sample that produces a distribution of incidence angles at the interfaces (which is a function of τ_s), hence the reflectivity at the interfaces is significantly different from that in the blank sample configuration. Therefore, the baseline practice cannot encompass the whole influence of geometrical optics for scattering samples.

7. Results

Using the model and methodology presented in previous sections, one can now:

- assess the range of optical thickness for which a given experimental setup actually measures the normal-hemispherical transmittance of a sample, by comparing results obtained with the device model φ and T_{NH} model ; the validity range of the three setups studied in this paper is produced in Sec. 7.1 below,

- look for a design of an experimental setup that would allow for recovering the T_{NH} experimentally; an illustration of this application is provided in Sec. 7.2,

- analyse measurements even outside the validity range of a setup, by using the device model rather than the T_{NH} model, either to validate radiative properties calculations or for inversion purposes ; this practice is illustrated in Section 7.3.

7.1. Validity range of the three studied experimental setups

This section aims at defining the validity range of each experimental setup presented in Section 2, *i.e.* the range of optical thicknesses for which the measured signal corresponds to the normal-hemispherical transmittance T_{NH}, with a given tolerance. This provides suggestions to researchers on the variety of samples that can be analyzed with respect to T_{NH} computations, in a given experimental setup; whereas more turbid samples must be analyzed with respect to the device model φ.

Non-absorbing samples. Figure 10 shows the relative difference between T_{NH} and the signal model φ for purely scattering media with asymmetry parameter $g = 0.9$ and $g = 0$. For $g = 0.9$, setting a 10% tolerance, the three experimental setups in Section 2.1 only measure normal-hemispherical transmittance within the optical thickness ranges $\tau_s \in [0; 0.25]$, $\tau_s \in [0; 0.10]$ and $\tau_s \in [0; 0.06]$ respectively (see Eq. 12 for τ_s definition) which corresponds to $T_{NH} > 0.93$, 0.97 and 0.98 respectively (see Fig. 8). For more turbid samples, radiation missing the integrating sphere entrance, or lost through the cuvette sides, is no longer negligible (see Sec. 6). For that reason, the use of standard $10 \times 40 \times 10$ mm cuvettes for measuring T_{NH} is quite limited. With $g = 0$, validity ranges are broader: $\tau_s \in [0; 0.5]$, $\tau_s \in [0; 0.25]$ and $\tau_s \in [0; 0.2]$ respectively (*i.e* $T_{NH} > 0.80$, 0.89 and 0.91 respectively), but still correspond to values of τ_S less than 1.

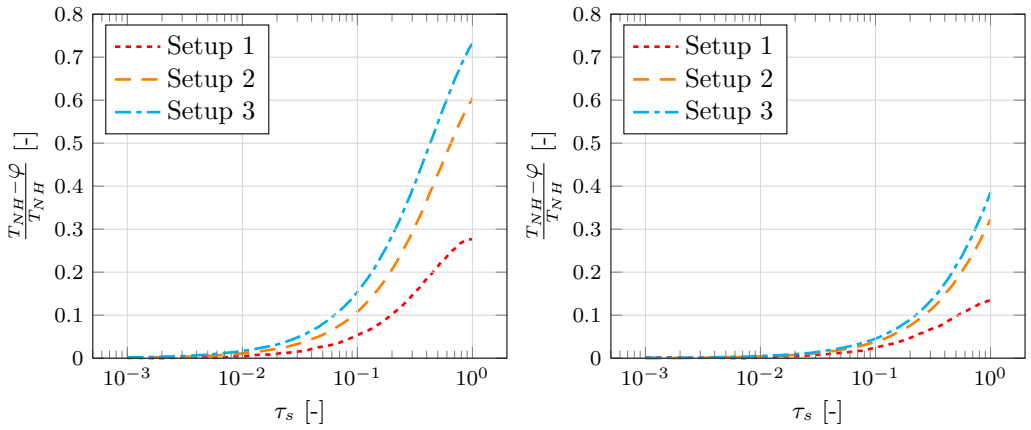

Figure 10: Validity range for purely scattering (non-absorbing) media. a) For $g = 0.9$ and b) for $g = 0$. Relative difference between simulated normal-hemispherical transmittance T_{NH} and device signal φ as a function of scattering optical thickness τ_s (see Eq. 12), for the three experimental setups presented in Sec. 2.1. Henyey-Greenstein phase function is used. 95% confidence interval of Monte Carlo calculations are always below 0.0015.

Absorbing and scattering samples. Figures 11, 12 and 13 show the relative difference between T_{NH} and the signal model φ for absorbing and scattering media, with $g = 0.9$, $g = 0.5$ and $g = 0$ respectively. It displays two-dimensional color maps as a function of scattering optical thickness $\tau_s = k_s E(1-g)$ (see Eq. 12) and absorption optical thickness $\tau_a = k_a E$. Setting a 10% tolerance, the three experimental setups in Section 2.1 only measure normal-hemispherical transmittance within the optical thickness regions colored white.

All three experimental setups do measure the T_{NH} for purely absorbing samples ($\tau_S = 0$), whatever the value τ_A. Then, the deviation increases with τ_S, and the validity ranges are approximately the same as the ones observed for non-absorbing samples. The relative difference increases up to 60% with the setup 2 and 80% with the setup 3 for $g = 0.9$. Although it remains less than 30% with the setup 1 thanks to the use of a larger integrating sphere, most part of the map indicates relative difference above 10% when $\tau_s > 0.25$. Note that this setup shows a validity range at large value of τ_S. This may be explained by the reflectivity of the integrating sphere (see Fig. 9b), which makes that T_{NH} and φ intersect at $\tau_S \simeq 3$, a feature which is not recovered in the two other setups (see Fig. 8). Regarding the influence of the asymmetry

parameter g, validity ranges for purely scattering media are not significantly influenced, but are extended as g decreases for absorbing media, especially with $g = 0$. However, most part of the maps still display a relative difference larger than 10%.

Hence the validity ranges are restricted to $\tau_S \ll 1$ for all the devices presented here, with less constraints on the value of τ_A. Meanwhile, by using the device model φ instead of T_{NH} for inversion procedures or radiative properties validation, it is possible to use these setups beyond their validity range, as illustrated in the next section.

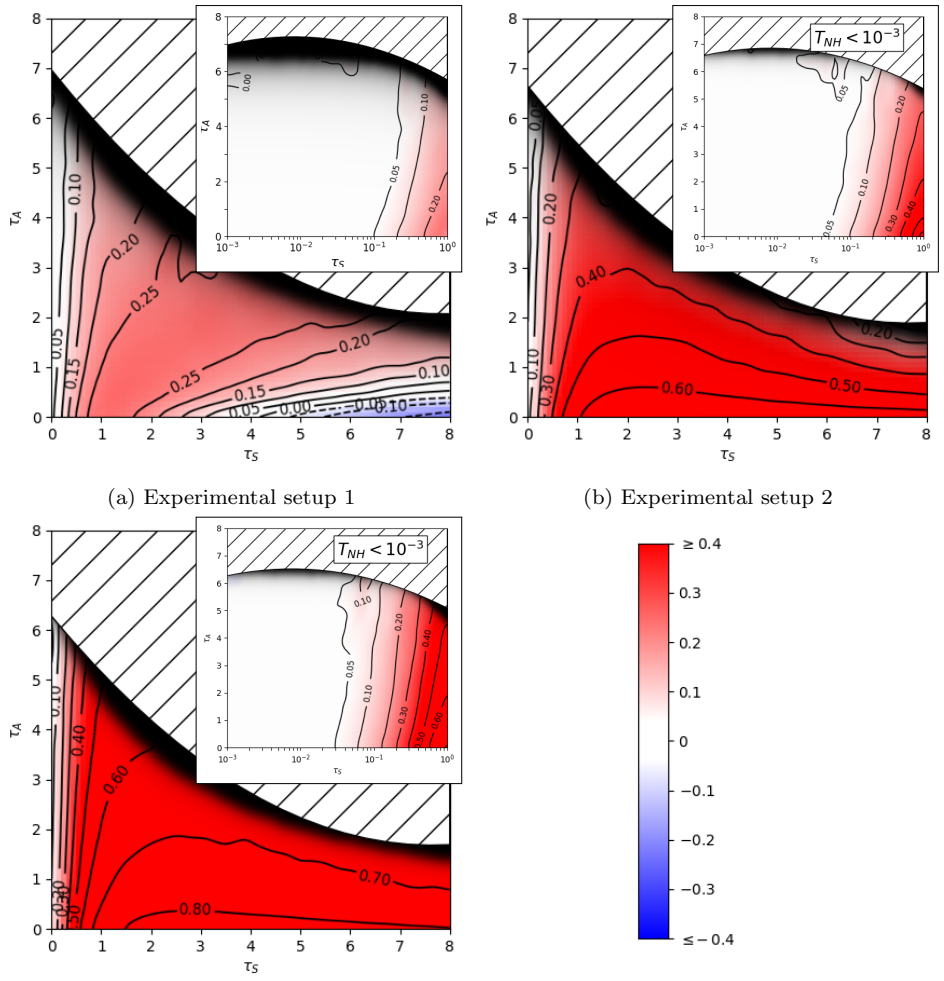

(a) Experimental setup 1

(b) Experimental setup 2

(c) Experimental setup 3

Figure 11: Validity range for absorbing and scattering samples with $g = 0.9$. Relative difference $\frac{T_{NH}-\varphi}{T_{NH}}$ (values indicated in the color bar at the bottom right) between simulated normal-hemispherical transmittance T_{NH} and device signal φ as a function of scattering optical thickness τ_s (see Eq. 12) and absorbing optical thickness $\tau_a = k_a E$, for the three experimental setups presented in Sec. 2.1. For each setup, a semilog zoom for low optical thicknesses is inserted at the top right. Henyey-Greenstein phase function is used. Regions where $T_{NH} < 10^{-3}$ are hatched, since the signal delivered by the instrument would be too weak to be analyzed. Blacked area are drawn when the Monte Carlo relative uncertainty is more than 10%, due to T_{NH} decreasing to 0.

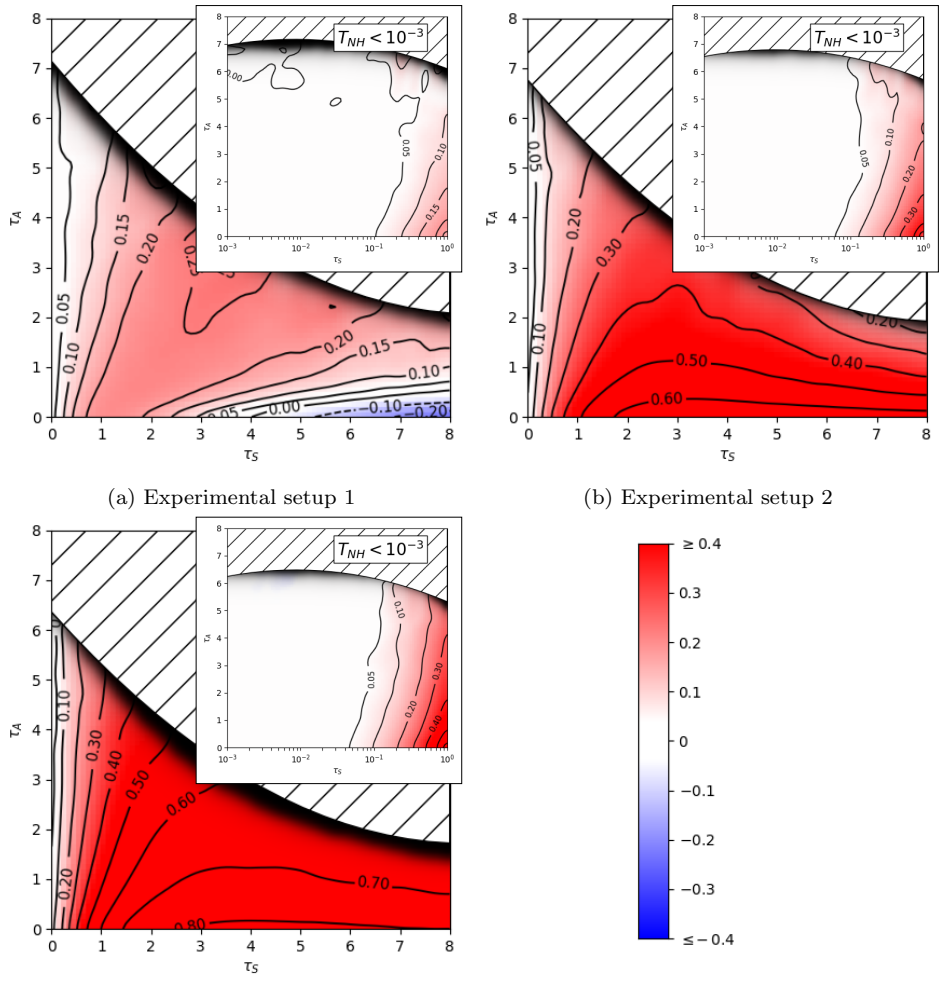

(a) Experimental setup 1

(b) Experimental setup 2

(c) Experimental setup 3

Figure 12: Validity range for absorbing and scattering samples with $g = 0.5$. Relative difference $\frac{T_{NH}-\varphi}{T_{NH}}$ (values indicated in the color bar at the bottom right) between simulated normal-hemispherical transmittance T_{NH} and device signal φ as a function of scattering optical thickness τ_s (see Eq. 12) and absorbing optical thickness $\tau_a = k_a E$, for the three experimental setups presented in Sec. 2.1. For each setup, a semilog zoom for low optical thicknesses is inserted at the top right. Henyey-Greenstein phase function with is used. Regions where $T_{NH} < 10^{-3}$ are hatched, since the signal delivered by the instrument would be too weak to be analyzed. Blacked area are drawn when the Monte Carlo relative uncertainty is more than 10%, due to T_{NH} decreasing to 0.

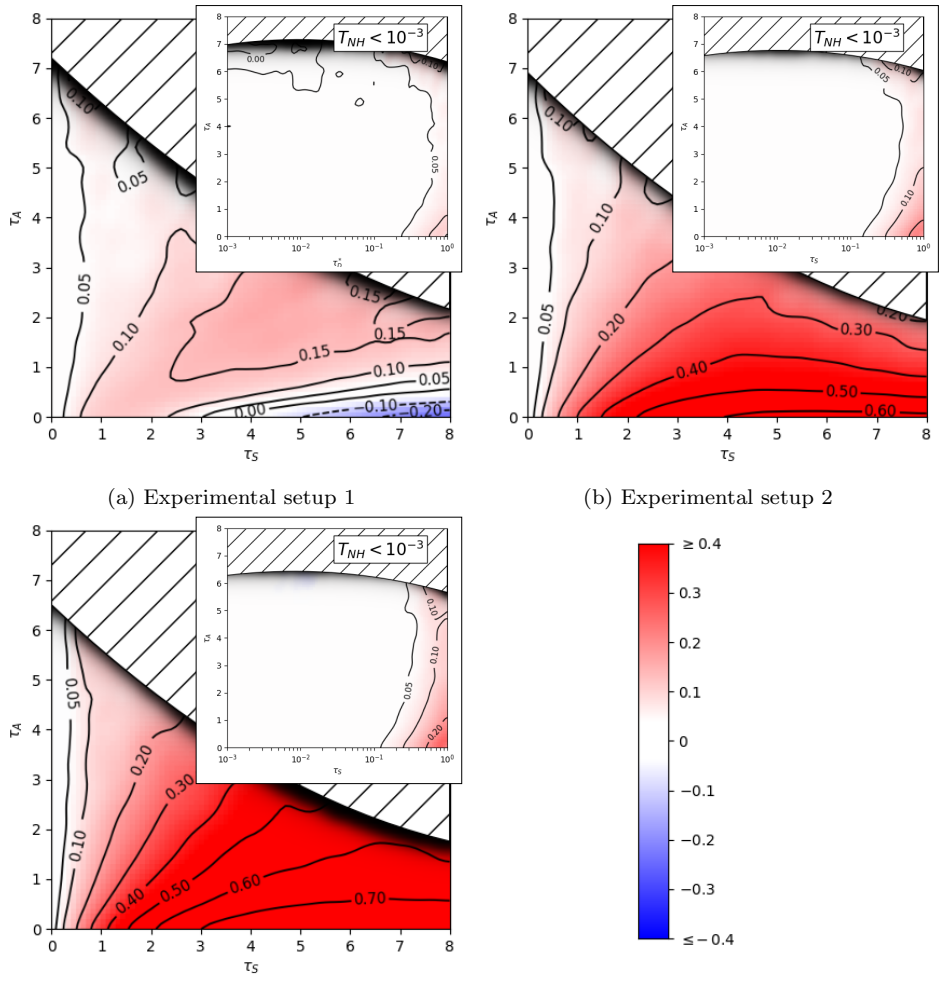

(a) Experimental setup 1

(b) Experimental setup 2

(c) Experimental setup 3

Figure 13: Validity range for absorbing and scattering samples with $g = 0$. Relative difference $\frac{T_{NH}-\varphi}{T_{NH}}$ (values indicated in the color bar at the bottom right) between simulated normal-hemispherical transmittance T_{NH} and device signal φ as a function of scattering optical thickness τ_s (see Eq. 12) and absorbing optical thickness $\tau_a = k_a E$, for the three experimental setups presented in Sec. 2.1. For each setup, a semilog zoom for low optical thicknesses is inserted at the top right. Henyey-Greenstein phase function is used. Regions where $T_{NH} < 10^{-3}$ are hatched, since the signal delivered by the instrument would be too weak to be analyzed. Blacked area are drawn when the Monte Carlo relative uncertainty is more than 10%, due to T_{NH} decreasing to 0.

7.2. Towards designing experimental setups

To design an experimental setup, the first thing to know is the working range of optical thickness. Here we have chosen to work with $\tau_S = 1$, and $g = 0.5$. Now, we would like to design an optical bench which measures the T_{NH} with a 5% accuracy: what should be the dimensions of the source, cuvette and integrating sphere?

We impose standard constraints on the design:

- the incident beam is a disk;
- the height of the cuvette is four times its width, as for commercial ones (see Figs. 3b, 4b);
- the entrance of the integrating sphere is a disk centered towards the source, whose diameter is 80% of the spanwise dimension of the cuvette;
- the diameter of the sphere is five times the diameter of the entrance (so that the entrance area is 1% of the surface of the sphere).

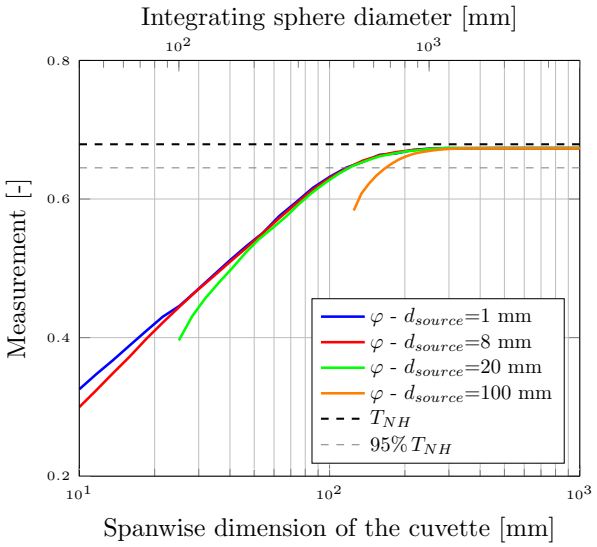

Figure 14: Signal delivered by the device as a function of the spanwise dimension of the cuvette, for several source beam diameters. Note that we have ignored the points where the diameter of the beam is larger than the entrance of the integrating sphere. T_{NH} signal is represented by the black dashed line.

Figure 14 shows the result of the device model as a function of the spanwise dimension of the cuvette (or equivalently, the integrating sphere diameter), for several diameters of the incident beam. In order to design an experimental device that would agree with the T_{NH} with a 5 % tolerance, the spanwise dimension should be larger than 125 mm, *i.e* a sphere entrance of 100 mm, for beam diameters between 1 and 20 mm (the required spanwise dimension is increased with larger source beams). However, this would lead to an integrating sphere diameter of 500 mm. Note that such large dimensions would raise two issues:

- large sphere diameters imply loss of signal due to multiple reflections in the sphere, hence a powerful source and a highly sensitive photomultiplier are required,
- large cuvettes imply increased volume of the sample (625 mL), which can be problematic if the stock of solution/particle is limited.

Meanwhile, thanks to the model developed in the present paper, it is possible to use optical benches with reasonable dimensions even when they do not measure the T_{NH}, as illustrated by two examples in the next section.

7.3. Illustration in two practical cases

Here we illustrate the practical implementation of our method in both the situations listed at the beginning of the introduction:

1. a validation of calculated radiative properties, in the case of semiconductor particles used in a photoreactor for solar fuel production,
2. a simple inversion of spectrophotometry measurements, in the case of the microalgae *Chlamydomonas reinhardtii*.

These illustrations emphases that it is now possible to use T_{NH} measurement devices outside of their validity range. We also discuss the radically different conclusions that we would have been drawn from those spectrophotometric campaigns if using T_{NH} calculation rather than our complete device model. Yet, implementations are performed on the experimental setup 1 (see Sec. 2.1) which has the widest validity range of the three studied devices.

7.3.1. Testing radiative properties of particles

Here we aim at validating the radiative properties of spherical particles of cadmium sulfide (CdS) synthesized in the Institut de Chimie de Clermont-Ferrand following the protocol described in [32]. These semi-conductor particles are used in a slurry photoreactor for solar fuel production. The validation of their radiative properties is of prime importance as radiative transfer is the first step of a whole model including charge transport and chemical reactions, that will be validated against solar fuel production in the photoreactor.

Figure 15 presents the comparison between experimental results, T_{NH} and the device model φ. If these results are analyzed on the assumption that the device measures T_{NH}, we conclude that the radiative properties calculated for the CdS particles are invalid above 500 nm (that is the semi-conductor bandgap). This conclusion would be wrong: according to Figs. 11a and 15b, what is observed is simply the validity range of the device. The spectrophotometer indeed measures T_{NH} below 500 nm, where the sample absorbs and scatters light moderately ($\tau_s < 0.25$), but we are outside its validity range when the sample is purely scattering with $\tau_s > 0.25$, above 500 nm.

In contrast, analyzing these results on the basis of the device model φ permits to draw some interesting conclusions. The calculated radiative properties are reasonably accurate over the whole spectrum with, however, a notable discrepancy around the bandgap ($\lambda \sim 500$ nm) which may be caused by the slit width (here 2 nm) or defects in the materials. Indeed, the presence of impurities or defects in the crystal structure leads to a broader bandgap for the synthesized material than for the perfect crystal from which the values of the refractive index have been obtained in [33]. Hence, thanks to the methodology described in the present article, we have been able to extend the spectrophotometer range of applications, to validate the radiative properties of semi-conductor particles and draw perspectives for a more accurate calculation of these properties.

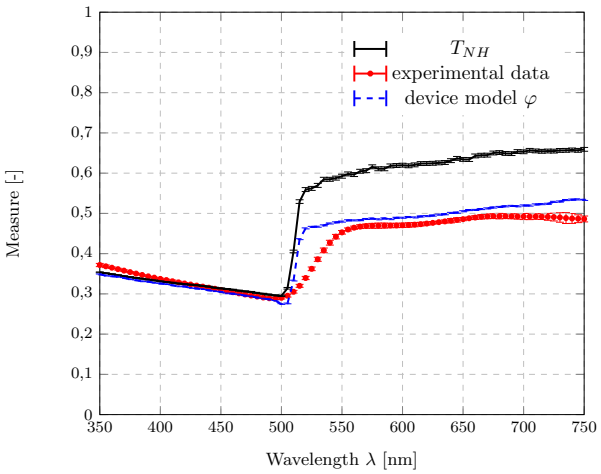

(a)

λ	400 nm	700 nm
τ_A [-]	0.97	0
τ_S [-]	0.18	1.09

(b)

Figure 15: Spectral validation of CdS particle radiative properties using the experimental device 1 (see Sec. 2.1). (a) Measurements and models. CdS particles have been characterized (size and shape) by scanning electron microscopy on a Zeiss Supra 55VP MEB. Particles are spherical, and their size distribution is lognormal with median diameter 328 nm and standard deviation 1.061. As particles are spherical, their radiative properties are computed according to Mie theory. Values of the real and imaginary part of the refractive index are obtained from [33]. The CdS particle suspension has concentration of 0.084 g/L. Altogether, this leads to the optical thicknesses provided in (b) for two wavelengths.

7.3.2. Particles refractive index determination by inversion

Here we revisit results obtained in 2015 (see the section 6.4 and Figure 11 in [6]) for the refractive index n of the spherical microalgae *Chlamydomonas reinhardtii* at 820 nm, where it does not absorb radiation (the imaginary par of the refractive index is zero). For that purpose a simple inversion was performed to determine the value $n_{820\,nm}$ insuring that experimental measurement $M_{exp,820\,nm}$ and calculated transmittance $T_{NH}(n)$ are equal. This inversion is relatively simple because, first, only one parameter is inverted, second, it is only performed for one microalgae suspension at one concentration and one wavelength, which implies that the criteria of equivalence is simply the equality $T_{NH}(n_{820\,nm}) = M_{exp,820\,nm}$. The direct model $T_{NH}(n)$ is implemented as follows: i) the value of n, the refractive index of water and the microalgae size distribution obtained from optical microscope image processing are the input parameters of the Lorenz–Mie code provided at `www.giss.nasa.gov/staff/mmishchenko`, which provides the radiative properties at $820\,nm$, ii) the T_{NH} for the sample length and concentration

is obtained as described in Sec. 3. Results are plotted in black in Fig. 16. With this approach, the inversion gives $n_{820\,nm} = 1.435$, which is quite high for a microalgae (as other researchers have pointed out in [4] in reaction to our results).

Now, we revisit these results by replacing the T_{NH} in the above procedure by the device model $\varphi(n)$ presented in the present article. The criteria of equivalence becomes $\varphi(n_{820\,nm}) = M_{exp,820\,nm}$. Results are plotted in blue in Fig. 16 and give $n_{820\,nm} = 1.39$, which is far more likely in the light of current knowledge about the volume fraction and refractive index of microalgae internal structures, as well as experimental measurement using nephelometers [4].

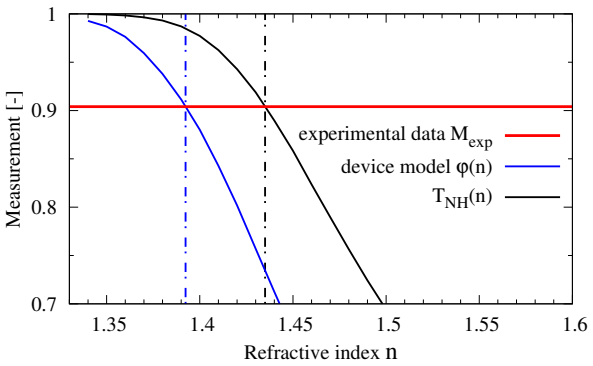

Figure 16: Inversion of *Chlamydomonas reinhardtii* refractive index at 820 nm. The sample is described in [6]: a suspension at $1\,g.L^{-1}$ of biomass (dry weight) is placed in the experimental setup 1 (see Sec. 2.1); the microalgae size distribution obtained from optical microscope image processing is lognormal with median radius $r_{eq} = 3.963\,\mu m$ and deviation $s = 1.18$; the average dry mass of one microalgae is $9.08 \times 10^{-14}\,kg$.

8. Conclusions

We investigated the range of validity of normal-hemispherical transmittance T_{NH} measurements on turbid samples using three representative optical benches : 1) a high accuracy setup using a large integrating sphere and large cuvette, 2) a standard commercial spectrophotometer with an integrating sphere accessory and 3) a prototype manufactured by PhotonLyX laboratory. Even the experimental setup 1 does not measure T_{NH} when scattering optical thickness τ_s exceeds 0.25 with $g = 0.9$ ($\tau_{s,max} = 0.1$ and 0.06 for

the two other devices) and when τ_s exceeds 0.5 with $g = 0$ ($\tau_{s,max} = 0.25$ and 0.2 for the two other devices). The implications are significant, and we illustrated the erroneous conclusions that can be drawn from using these devices outside their range of validity, either when validating calculated radiative properties, or when inverting particles refractive index. The correct radiative transfer model should be used to interpret the experiment measurement. If the physical problem clearly violates the 1D model, its use should be avoided.

However, we showed that using a complete radiative transfer model accounting for the geometry of the experimental setups, it is still possible to use a spectrophotometer or any optical bench even when it does not measure T_{NH}. Note that the analyses of our model indicates that the effect of geometrical optics is not canceled by implementing the standard baseline practice during experiments on turbid samples (*i.e.* using a cuvette filled with solvent only as a blank sample). Both the geometry of the instrument and geometrical optics must be described in the device model.

The computer code used to solve our model is made freely available at [19]. It uses recent advances in the computer graphics field, that enable to solve at low numerical cost the radiative transfer equation in any complex geometry, with open-source tools. A key property of this programming approach is the orthogonality between the Monte Carlo code solving the equations and the data describing the scene (surfaces and their properties, provided by the user). Thus, it is straightforward to implement the same model resolution for *any* experimental setup, as soon as its geometry is defined in a CAD file.

This offers two perspectives: first, the complexity of designing an instrument that measures T_{NH} for turbid media can be reported to the model, while ensuring the same quality of data analyses as if measuring T_{NH}. In other words, any spectrophotometer can now be used even for highly scattering samples. Second, the availability of fast calculations that are orthogonal to the geometric data allows for considering to run inversion procedures to design experimental setups adapted to specific applications (as for example in [14]).

Acknowledgements

This work was supported by the International Research Center "Innovation Transportation and Production Systems" of the I-SITE CAP 20-25. The authors sincerely thank all our colleagues at Institut de Chimie de

Clermont-Ferrand / Sigma-Clermont (France) : Audrey Potdevin, Damien Boyer, Pierre Martin and Genevieve Chadeyron for their invaluable help in synthesizing spherical CdS particles and for the time invested in scientific exchanges on artificial photosynthesis. We are also indebted to the staff of the Sigma-Clermont/Chemistry platform, in particular Cécile Esparcieux and Safia Laid, who kindly provided us with a commercial Shimadzu spectrophotometer with integrating sphere. Our sincere thanks also go to Guillaume Cogne of the GEPEA laboratory (Nantes/St Nazaire, France), who took time out to make measurements and provide geometric data on another commercial Agilent spectrophotometer (results not presented in this article). Finally, the authors also acknowledge the CNRS research federation FedESol where fecund discussions and debates take place since 2012.

References

[1] E. Ribeiro, G. Plantard, J.-F. Cornet, F. Gros, C. Caliot, V. Goetz, Experimental and theoretical coupled approaches for the analysis of radiative transfer in photoreactors containing particulate media: Case study of TiO2 powders for photocatalytic reactions, Chemical Engineering Science 243 (2021) 116733. doi:https://doi.org/10.1016/j.ces.2021.116733.
URL https://www.sciencedirect.com/science/article/pii/S0009250921002980

[2] E. Ribeiro, G. Plantard, J.-F. Cornet, F. Gros, C. Caliot, V. Goetz, AC/TiO2 granular photocatalysts optical properties: Material composition effect on the radiative transfer in a photoreactor, International Journal of Thermal Sciences 187 (2023) 108151. doi:https://doi.org/10.1016/j.ijthermalsci.2023.108151.
URL https://www.sciencedirect.com/science/article/pii/S1290072923000121

[3] L. Pilon, H. Berberoğlu, R. Kandilian, Radiation transfer in photobiological carbon dioxide fixation and fuel production by microalgae, Journal of Quantitative Spectroscopy and Radiative Transfer 112 (17) (2011) 2639–2660. doi:https://doi.org/10.1016/j.jqsrt.2011.07.004.
URL https://www.sciencedirect.com/science/article/pii/S002240731100269X

Nomenclature

λ	wavelength in vacuum $[m]$
A_0	area of the emission surface $[m^2]$
$\rho_{i\to j}$	reflectivity at an interface, for radiation coming from medium i to medium j [-]
$\rho_{S,\lambda}$	spectral reflectivity of the sensor [-]
τ_s	scattering optical thickness [-]
$\varphi = \frac{Q^{abs}_{sample}}{Q^{abs}_{sample}}$	Signal delivered by the spectrophotometer = device model [-]
$\boldsymbol{\omega}$	direction vector
$\boldsymbol{x}$	position vector
C_m	mass concentration $[\frac{kg}{m^3}]$
E	thickness of a slab ; light path of a cuvette [m]
g	asymmetry coefficient [-]
$I_\lambda(\boldsymbol{x}, \boldsymbol{\omega})$	light intensity $[mol_{h\nu}.s^{-1}.m^{-2}.sr^{-1}.nm^{-1}]$
$k_{a,\lambda} = \sigma_{a,\lambda} \times C$	spectral absorption coefficient $[m^{-1}]$
$k_{s,\lambda} = \sigma_{s,\lambda} \times C$	spectral scattering coefficient $[m^{-1}]$
n_i	refractive index of the medium i [-]
p_r	distribution function of reflected light [-]
Q^{abs}_{blank}	radiative flux absorbed at the sensor for the baseline experiment using a blank sample (cuvette containing the solvent only) [W]
Q^{abs}_{sample}	radiative flux absorbed at the sensor for the experiment on the sample [W]
$Q_{0,\lambda}$	spectral power of the source $[W]$
c	Speed of light in a vacuum
h	Planck constant
CAD	Computer-Aided Design

[4] F. R. F. Ballestas, M. Titica, J. Legrand, L. Pilon, G. Cogne, Prediction of the radiation characteristics and the light absorption rate of chlamydomonas reinhardtii cultivated under a progressive nitrogen starvation and accumulating carbon reserves, Journal of Quantitative Spectroscopy and Radiative Transfer 309 (2023) 108708. doi:https://doi.org/10.1016/j.jqsrt.2023.108708.
URL https://www.sciencedirect.com/science/article/pii/

S0022407323002261

[5] J. Dauchet, J.-F. Cornet, F. Gros, M. Roudet, C.-G. Dussap, Chapter one - photobioreactor modeling and radiative transfer analysis for engineering purposes, in: J. Legrand (Ed.), Photobioreaction Engineering, Vol. 48 of Advances in Chemical Engineering, Academic Press, 2016, pp. 1–106. doi:https://doi.org/10.1016/bs.ache.2015.11.003.
URL https://www.sciencedirect.com/science/article/pii/S0065237715000162

[6] J. Dauchet, S. Blanco, J.-F. Cornet, R. Fournier, Calculation of the radiative properties of photosynthetic microorganisms, Journal of Quantitative Spectroscopy and Radiative Transfer 161 (2015) 60–84. doi:https://doi.org/10.1016/j.jqsrt.2015.03.025.
URL https://www.sciencedirect.com/science/article/pii/S0022407315001272

[7] M. I. Cabrera, O. M. Alfano, A. E. Cassano, Absorption and scattering coefficients of titanium dioxide particulate suspensions in water, J. Phys. Chem 100 (1996) 20043–20050. doi:10.1021/jp962095q.

[8] A. E. Cassano, O. M. Alfano, Reaction engineering of suspended solid heterogeneous photocatalytic reactors, Catalysis Today 58 (2000) 167–197. doi:10.1016/S0920-5861(00)00251-0.

[9] S. A. Prahl, M. J. C. van Gemert, A. J. Welch, Determining the optical properties of turbid media by using the adding-doubling method., Applied optics 32 (1993) 559. doi:10.1364/AO.32.000559.

[10] Y. Qin, P. Tian, L. Zhao, S. M. Mutisya, J. Jin, J. Q. Lu, X. H. Hu, Robustness of inverse solutions for radiative transfer parameters from light signals measured with different detection configurations, Journal of Quantitative Spectroscopy and Radiative Transfer 274 (2021) 107883. doi:10.1016/J.JQSRT.2021.107883.

[11] B. W. Xie, L. X. Ma, J. M. Zhao, L. H. Liu, X. Z. Wang, Y. R. He, Experimental study of the radiative properties of hedgehog-like ZnO–Au composite particles, Journal of Quantitative Spectroscopy and Radiative Transfer 232 (2019) 93–103. doi:10.1016/J.JQSRT.2019.05.006.

[12] Y. Zhang, X. Wen, Z. Xu, D. Zhu, The accuracy of a commercial spectrophotometer with single integrating sphere for measuring optical properties of turbid sample, in: E. D. Jansen, R. J. Thomas (Eds.), Optical Interactions with Tissues and Cells XXI, Vol. 7562, International Society for Optics and Photonics, SPIE, 2010, p. 756219. doi:10.1117/12.841821.
URL https://doi.org/10.1117/12.841821

[13] H. Berberoglu, L. Pilon, Experimental measurements of the radiation characteristics of anabaena variabilis ATCC 29413-u and rhodobacter sphaeroides ATCC 49419, International Journal of Hydrogen Energy 32 (18) (2007) 4772–4785. doi:https://doi.org/10.1016/j.ijhydene.2007.08.018.
URL https://www.sciencedirect.com/science/article/pii/S0360319907005034

[14] L. Brunel, Chapter 5 Measure of Optical Properties of Paper when Wetting Using Monte-Carlo Inversion, EDP Sciences, Les Ulis, 2023, Ch. 5, pp. 51–62. doi:doi:10.1051/978-2-7598-2931-6.c006.
URL https://doi.org/10.1051/978-2-7598-2931-6.c006

[15] M. Jonasz, G. R. Fournier, Chapter 4 - measurements of light scattering by particles in water, in: M. Jonasz, G. R. Fournier (Eds.), Light Scattering by Particles in Water: Theoretical and Experimental Foundations, Academic Press, Amsterdam, 2007, pp. 145–265. doi:https://doi.org/10.1016/B978-012388751-1/50004-1.
URL https://www.sciencedirect.com/science/article/pii/B9780123887511500041

[16] D. Stramski, J. Piskozub, Estimation of scattering error in spectrophotometric measurements of light absorption by aquatic particles from three-dimensional radiative transfer simulations, Appl. Opt. 42 (18) (2003) 3634–3646. doi:10.1364/AO.42.003634.
URL https://opg.optica.org/ao/abstract.cfm?URI=ao-42-18-3634

[17] F. Bevilacqua, A. J. Berger, A. E. Cerussi, D. Jakubowski, B. J. Tromberg, Broadband absorption spectroscopy in turbid media by combined frequency-domain and steady-state methods, Appl. Opt.

39 (34) (2000) 6498–6507. doi:10.1364/AO.39.006498.
URL https://opg.optica.org/ao/abstract.cfm?URI=ao-39-34-6498

[18] F. Foschum, Broadband absorption spectroscopy of turbid media using a dual step steady-state method, Journal of Biomedical Optics 17 (3) (2012) 037009. doi:10.1117/1.jbo.17.3.037009.
URL https://www.spiedigitallibrary.org/terms-of-use

[19] Starlyx, monte-carlo simulation for complex scenes and optical instruments, www.starlyx.org.

[20] M. Pharr, et al., Physically Based Rendering: From Theory to Implementation, 3rd Edition, Morgan Kaufmann Publishers Inc., 2016.

[21] I. Georgiev, T. Ize, M. Farnsworth, R. Montoya-Vozmediano, A. King, B. V. Lommel, A. Jimenez, O. Anson, S. Ogaki, E. Johnston, et al., Arnold: A brute-force production path tracer, ACM Transactions on Graphics (TOG) 37 (3) (2018) 1–12. doi:10.1145/3182160.

[22] meso-star (www.meso star.com), star-engine.
URL https://gitlab.com/meso-star/star-engine

[23] I. Wald, S. Woop, C. Benthin, G. S. Johnson, M. Ernst, Embree: a kernel framework for efficient cpu ray tracing, ACM Transactions on Graphics (TOG) 33 (4) (2014) 1–8. doi:10.1145/2601097.2601199.

[24] J. Dauchet, G. Foin, L. Brunel, J.-F. Cornet, F. Gros, T. Vourc'h, Donnees de replication pour : Extending the use of normal hemispherical transmittance (T_{NH}) measurements by modelling 3d multiple scattering radiative transfer (2024). doi:10.57745/BVMFZ1.
URL https://doi.org/10.57745/BVMFZ1

[25] J. R. Howell, M. P. Mengüç, K. Daun, R. Siegel, Thermal radiation heat transfer, CRC press, 2020.

[26] Freecad, https://www.freecad.org/, v 0.19 (2023).

[27] B. O. Community, Blender - a 3D modelling and rendering package, Blender Foundation, Stichting Blender Foundation, Amsterdam (2018).
URL http://www.blender.org

[28] I. H. Malitson, Interspecimen comparison of the refractive index of fused silica, Journal of the Optical Society of America 55 (1965) 1205–1209. doi:10.1364/JOSA.55.001205.

[29] N. G. Sultanova, et al., Measuring the refractometric characteristics of optical plastics, Optical and Quantum Electronics 35 (2003) 21–34. doi:10.1023/A:1021811200953.

[30] I. Thormählen, et al., Refractive index of water and its dependance on wavelength, temperature and density, Physical and Chemical Reference Data 14 (1985) 933–945. doi:10.1063/1.555743.

[31] D. J. Segelstein, The complex refractive index of water, Ph.D. thesis, University of Missouri - Kansas City (1981).
URL http://hdl.handle.net/10355/11599

[32] B. Chai, M. Xu, J. Yan, Z. Ren, Remarkably enhanced photocatalytic hydrogen evolution over mos 2 nanosheets loaded on uniform cds nanospheres, Applied Surface Science 430 (2017) 523–530. doi:10.1016/j.apsusc.2017.07.292.

[33] S. Adachi, Handbook on Physical Properties of Semiconductors, Kluwer Academic Publishers, 2004. doi:10.1007/1-4020-7821-8.